Measurement of X-ray Absorption Spectra for a Range of Chemical Elements

Usama Ahmed, Rajan Kholia, Amit Sen

Duration of Experiment : 11/02/20 – 10/03/20

Location: Department of Physics and Astronomy, University College London, Gower Street, London WC1E 6BT

Word count: 3150

Abstract

X-ray spectroscopy is a powerful and non-destructive technique that is uninfluenced by the chemical environment of an element. Herein, the X-ray absorption spectra for various elements is studied and calculations for mass absorption coefficient and its dependency on wavelength and atomic number are elucidated. Moseley's law is verified for both K and L-shell absorption edges and values for the Rydberg and screening constant are calculated. Comparisons to accepted literature values are provided and reasons for disagreements explored.
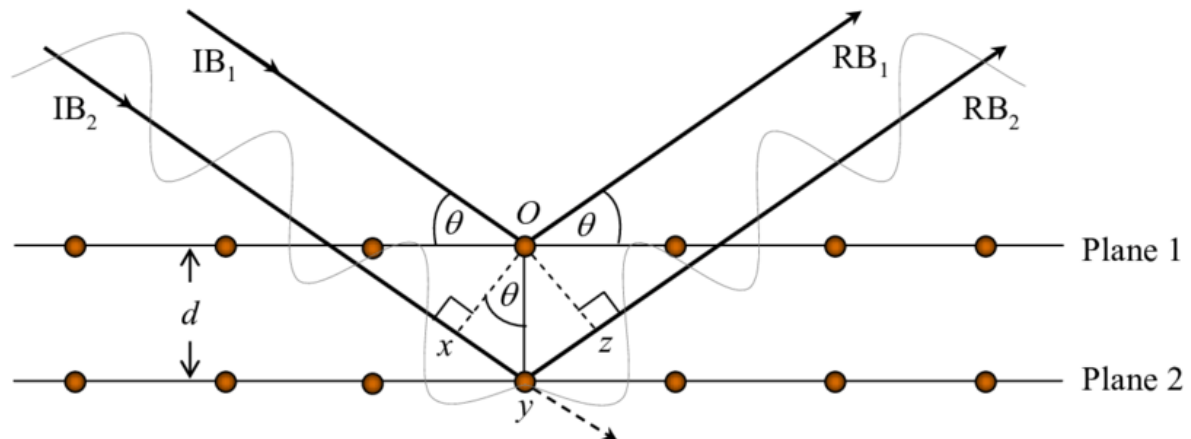
1   Introduction

Figure 1 : Schematic illustration of Bragg's Law where $IB_{1/2}$ are incoming beams and $RB_{1/2}$ are the reflected beams from miller planes with spacing d[12].

X-rays can be produced when electrons in the inner shells of atoms are ionised, typically via collision of high energy electrons, leaving a "core vacancy", an outer shell electron then falls into the core, emitting radiation that is typically in the x-ray spectrum[1], shown in figure 2. Since these transitions typically take place from the inner n = 1, 2, 3 shells, this emitted radiation is unique to the element and is unaffected by its chemical surroundings and is therefore known as the element's characteristic x-ray emission spectrum. The emitted radiation can be characterised via a diffraction grating (or planes of a single crystal) where Bragg's law gives the relationship between the Bragg angle and the wavelength of the incident radiation, shown in figure 1.
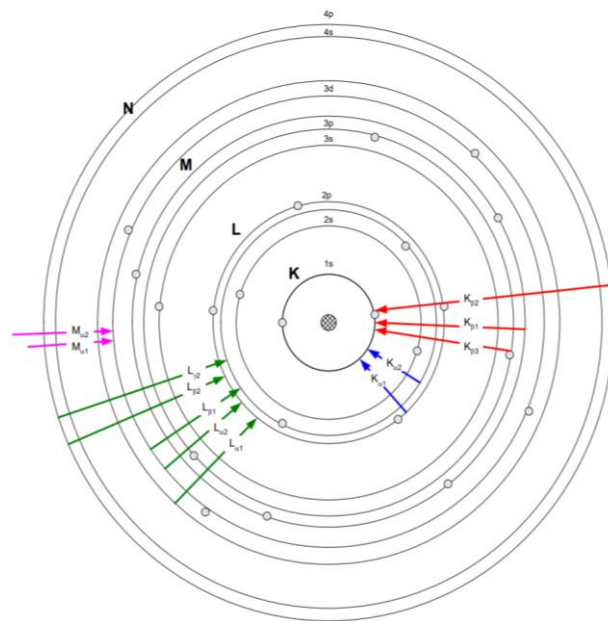

Figure 2 : Schematic illustration of various K, L and M transitions[13]

2   Equipment and Methodology

Figure 3 : PHYWE XR 4 V1.4 X-ray spectroscopy unit[14]

All measurements are carried out using a PHYWE XR 4 V1.4 X-ray spectrometer with a tungsten x-ray source. The x-ray tube voltage is set to 30kV with a current of 1.0mA. The Geiger-Muller counter voltage is set to 500 V. The goniometer is auto-calibrated every time a sample is placed or removed from the goniometer. A collimator of width 2mm is used for the solid samples placed in the sample holder and 5mm for pre-prepared powdered sample discs fastened to the front of the collimator. The equipment takes a measure of the count rate (number of ionizing radiation particles detected by the GM (Geiger-Muller) counter every second) pre-set angles before moving on by a pre-set angular increment. Here, the coupled θ/2θ scan mode is used, which keeps the detector at the correct angle for any "peaks", with time steps of 2s, 4s and 60s at various points in the experiment. Angular increments of 0.1° are used for all measurements. The resolving power of the spectrometer is calculated using LiF and KBr as single crystal analysers. All experimental results, otherwise, are obtained using LiF single crystal analyser. Samples used for measurements are discs of thin sheet Al and Zn of thicknesses 0.02mm, 0.04mm, 0.06mm, 0.08mm and 0.01mm, Sn, Cu and Ni of thickness 0.025mm and discs of pre-prepared powdered Zn, Ag, W and Au with a thickness between 0.2mm and 0.4mm. The sheet samples are placed in the sample holder on the goniometer while the powdered samples are fastened to the front of the collimator with blu-tack.

The GM tube is a gaseous ionizing detector. Incident radiation ionises the inert gas in the GM tube, producing a small electrical discharge, amplified by the Townsend discharge[2] effect. The GM counter collects these discharged particles and detects them when a drop in the voltage is produced, as the particles strike the electrodes. During this drop, however, the counter cannot detect any more particles and needs to recharge. This produces a "dead time" where no particles are detected and can be a problem if high energy radiation is incident. To counter this, the "true count", shown by equation 2, is calculated and used in all data analysis.

$$N = \frac{N_0}{(1-\tau N_0)} \qquad (1)$$

The resolving power of the spectrometer is obtained via plotting θ against calculated λ. The gradient gives the angular dispersion, shown in equation 2[4]. The resolving power is the product of angular dispersion and beam width.

$$\frac{\Delta\theta}{\Delta\lambda} = \frac{n}{2d\cos\theta} \qquad (2)$$

The value of the linear absorption coefficient depends on the incident radiation energy and varies with the atomic number of the target. Over ranges of wavelength that do not include an absorption edge, the absorption coefficient is proportional to $\lambda^3 Z^3$, but can otherwise be calculated using equation 3.

$$I = I_0 e^{-\mu t} \qquad (3)$$

Where μ is the mass absorption coefficient defined as $\frac{\mu}{\rho}$ i.e. linear absorption coefficient over material density, and I is the count rate. I_0 is the background count rate in the absence of a sample.

Moseley's Law[3] is an empirical law relating the binding energy of an electron to the atomic number of the element, shown in equations 4 and 5.

$$E_n = \frac{me^4}{8\varepsilon_0^2 h^2} (Z - \sigma)^2 \frac{1}{n^2} \qquad (4)$$

$$\frac{1}{\lambda} = R(Z - \sigma)^2 \frac{1}{n^2} \qquad (5)$$

Where R is Rydberg's constant, σ is the screening constant and n is the quantum number.

Converting Bragg angle θ into energy (eV) requires use of equation 6, for first order (n=1) reflections,

$$eV = \frac{hc}{2de\sin(\theta)} \qquad (6)$$

where e is the charge of an electron.

3   Results and Discussion

In order to elucidate the resolving power of the spectrometer and confirm the X-ray source, the spectrometer is run with nothing in the sample holder and either LiF (d = 201 pm) or KBr (d = 329 pm) as the single crystal analyser. Measurements of the count rate from $\theta = 4.0°$ to $\theta = 35.0°$ with a counting time of 2s per step are taken and plots of the true count rate (#/s) against calculated incident radiation energy (keV) using are shown in figure 5.
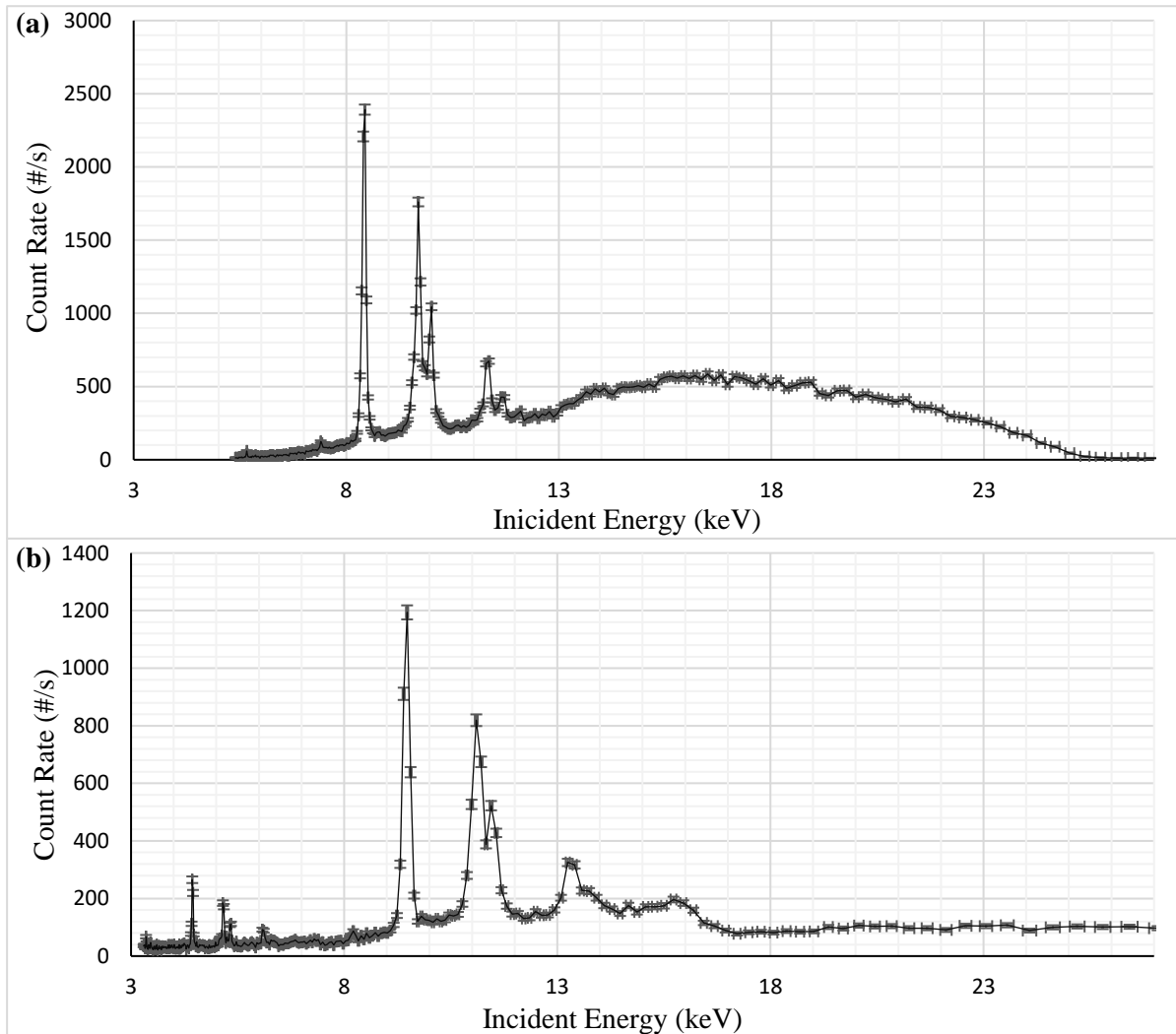

Figure 5 : X-ray spectra of Tungsten using (a) LiF and (b) KBr as single crystal analysers

Literature values for tungsten L-peaks occur in the 8-13 keV region[5]. Both spectra show 4 clear peaks in the region of interest. The X-ray spectra using the KBr analyser does not show significant Bremsstrahlung radiation and is overall shifted to the right, compared to the LiF spectra. Bremsstrahlung radiation occurs from the deacceleration of the incident high energy photons when they hit the target tungsten atoms, in the X-ray source tube.

The accepted characteristic spectrum of Tungsten shows 5 peaks corresponding to the L-shell transitions. The spectrometer is run again with a higher step count of 4s around the peaks in figure 5 to

obtain higher accuracy data with none of the peaks resolving into more than one wavelength. The energies of the experimental peaks and the corresponding literature values are shown in table 1.

The peaks at (8.44 ± 0.01) keV and (9.48 ± 0.02) keV in the LiF and KBr spectra respectively, correspond to the strong tungsten $L\alpha_1$ and $L\alpha_2$ peaks but are not resolved into two peaks on the obtained spectra.

Seignbahn / IUPAC notation	Literature[6] Characteristic Lines (keV)	Characteristic Lines - LiF	Characteristic Lines - KBr
$L\alpha_1$ / L_3-M_5	8.3976	8.44 ± 0.01	9.48 ± 0.02
$L\alpha_2$ / L_3-M_4	8.3352		
$L\beta_1$ / L_2-M_4	9.67235	10.01 ± 0.02	11.09 ± 0.03
$L\beta_2$ / L_3-N_5	9.9615	9.72 ± 0.02	11.45 ± 0.04
$L\gamma_1$ / L_2-N_4	11.2859	11.36 ± 0.02	11.27 ± 0.05

Table 1 : Experimental and Literature[6] energy Values in keV of the characteristic L-peaks of Tungsten using LiF and KBr analysers

Use of an LiF single crystal analyser shows better agreement with literature values than KBr.

To determine the resolving power of the spectrometer, Bragg angle (°) was plotted against calculated wavelength using the Bragg equation. This gives a straight-line graph, the gradient of which is the angular dispersion value shown in equation 2. Resolving powers in table 2 were calculated by using stated collimator widths of 2mm and 5mm. Table 2 shows a higher resolving power of the LiF single crystal analyser and therefore better ability to distinguish closely spaced peaks. The LiF analyser is used for all subsequent measurements. Better agreement should be seen for experimentally determined beam widths which change as they leave the collimator.

	Crystal Analyser	2mm collimator width(°)	5mm collimator width (°)
Resolving Power	KBr	$(1.860 \pm 0.003) \times 10^8$	$(4.650 \pm 0.007) \times 10^8$
	LiF	$(3.044 \pm 0.004) \times 10^8$	$(7.61 \pm 0.01) \times 10^8$

Table 2 : Resolving Power of the X-ray spectrometer using LiF and KBr single crystal analysers with a 2mm and a 5mm collimator width

To determine the mass absorption coefficient, 20 consecutive measurements of the count rate, with a step time of 2s, from $\theta = 9.8°$ to $\theta = 10.2°$, corresponding to 17.81 ± 0.05 keV, in the background away from any strong peaks, and $\theta = 21.2°$ and $\theta = 21.8°$, corresponding to a strong $L\alpha$ peak of 8.44 ± 0.01 keV were taken with different thicknesses of Aluminium and Zinc in the sample holder. A plot of the natural logarithm of the average count rate I, with the sample, divided by the background count rate I_0, without the sample, against the corresponding thickness is shown in figures 6 and 7. Experimentally

obtained mass absorption coefficients of Zn and Al at a background (B) energy of 17.81 ± 0.05 keV and Lα (L) energy of 8.44 ± 0.01 keV are shown in table 3 along with the accepted literature values.
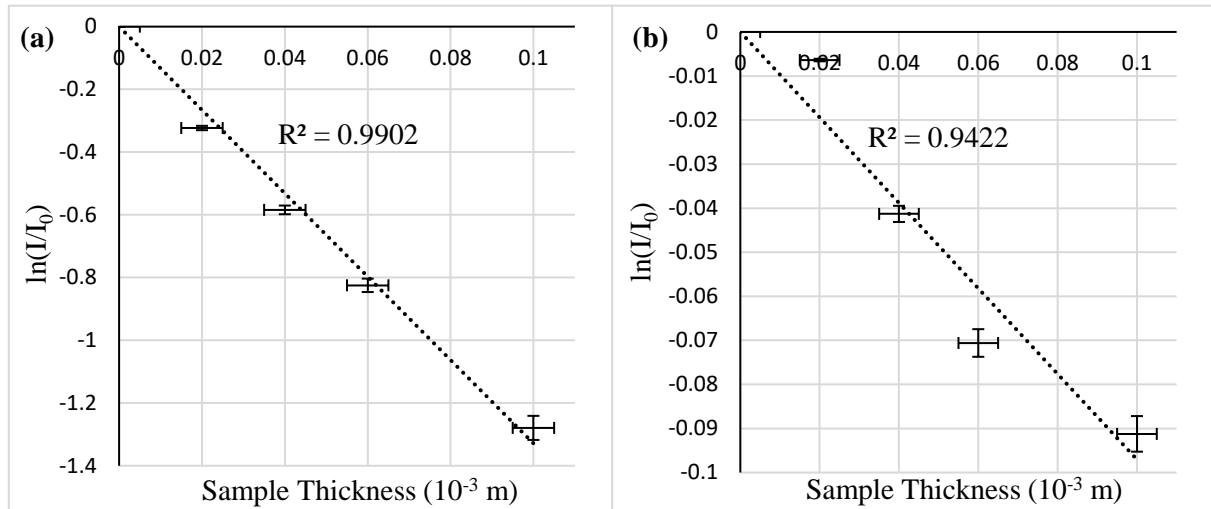

Figure 6 : $\ln(I/I_0)$ against sample thickness for Aluminium at (a) 21.5° and (b) 10° with a line of best fit (dotted) and associated R^2 coefficient of determination

The mass absorption coefficient is simply the gradient of the plots in figures 6 and 7, divided by the density of the element, with Al and Zn having densities of 2.70 gcm^{-3} and 7.14 gcm^{-3} at room temperature respectively[7], [8].

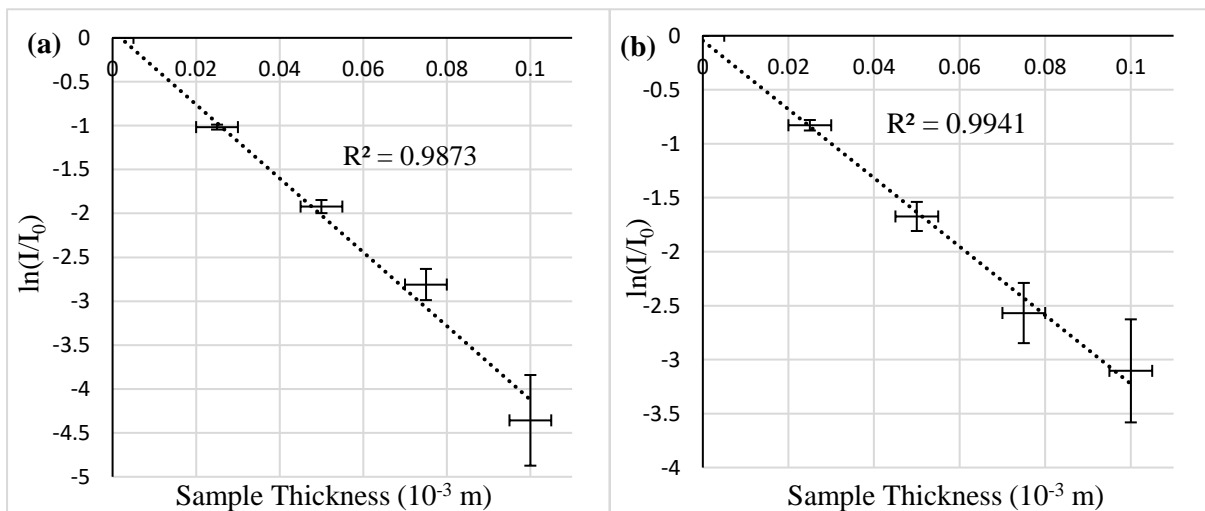Figure 7 : $\ln(I/I_0)$ against sample thickness for Zinc at (a) 21.5° and (b) 10° and R^2 coefficient

Sample	Mass Coefficient (cm^2g^{-1}) (Exp)	Mass Coefficient (cm^2g^{-1}) (Lit)
Al – B	3.7 ± 0.4	3.062
Al – L	47 ± 2	51.082
Zn – B	45 ± 2	59.18
Zn – L	59 ± 4	61.96

Table 3 : Experimental mass coefficient (Exp) values of Al and Zn at incident energy of (L) 8.44 ± 0.01 keV and (B) 17.81 ± 0.05 keV compared with the associated literature (Lit) values [15], [16]

Literature value for Zn – L lies within experimental uncertainties showing good agreement. Poor agreement is seen with other values, particularly Zn – B.

Accepted literature values for the K-absorption edge for are 1.559 keV for Aluminium and 9.661 keV for Zn[9]. This can be used to rationalise the results seen in table 3, which show good agreement with literature for Zn – L, but poor agreement otherwise. Incident energy of 17.81 ± 0.05 keV is far from any absorption edges in Aluminium, giving a low mass absorption coefficient while energies of 17.81 ± 0.05 keV and particularly 8.44 ± 0.01 keV return large mass absorption coefficients for Al and Zn. The absorption coefficient varies rapidly with incident energy around absorption edges and this is can be seen from the large experimental uncertainties and poor agreement with literature values.

The mass absorption coefficients of Sn, Ni and Cu as a function of wavelength were calculated by taking measurements of count rate from $\theta = 6°$ to $\theta = 25°$ with a step time of 60s using a sample thickness of 0.025mm. The mass absorption coefficient was calculated via use of equation 3 and plotted against incident $\lambda^3 Z^3$, as shown in figure 8. The gradient was calculated over the linear region of the plots and compared to literature values to ascertain the dependency of the mass absorption coefficient on wavelength and atomic number. Table 4 shows the gradients over the $\theta = 6°$ to $\theta = 16°$ region and associated literature values.

	Experimental Gradient (cm^2g^{-2})	Literature Value (cm^2g^{-2})[5]
Cu	$(4.1 \pm 0.1) \times 10^{27}$	4.66×10^{27}
Ni	$(5.7 \pm 0.3) \times 10^{26}$	4.90×10^{26}
Sn	$(1.1 \pm 0.8) \times 10^{27}$	2.28×10^{27}

Table 4 : Rate of change of the mass coefficient with increasing incident wavelength (experimental gradient) obtained from figure 8 and corresponding literature values
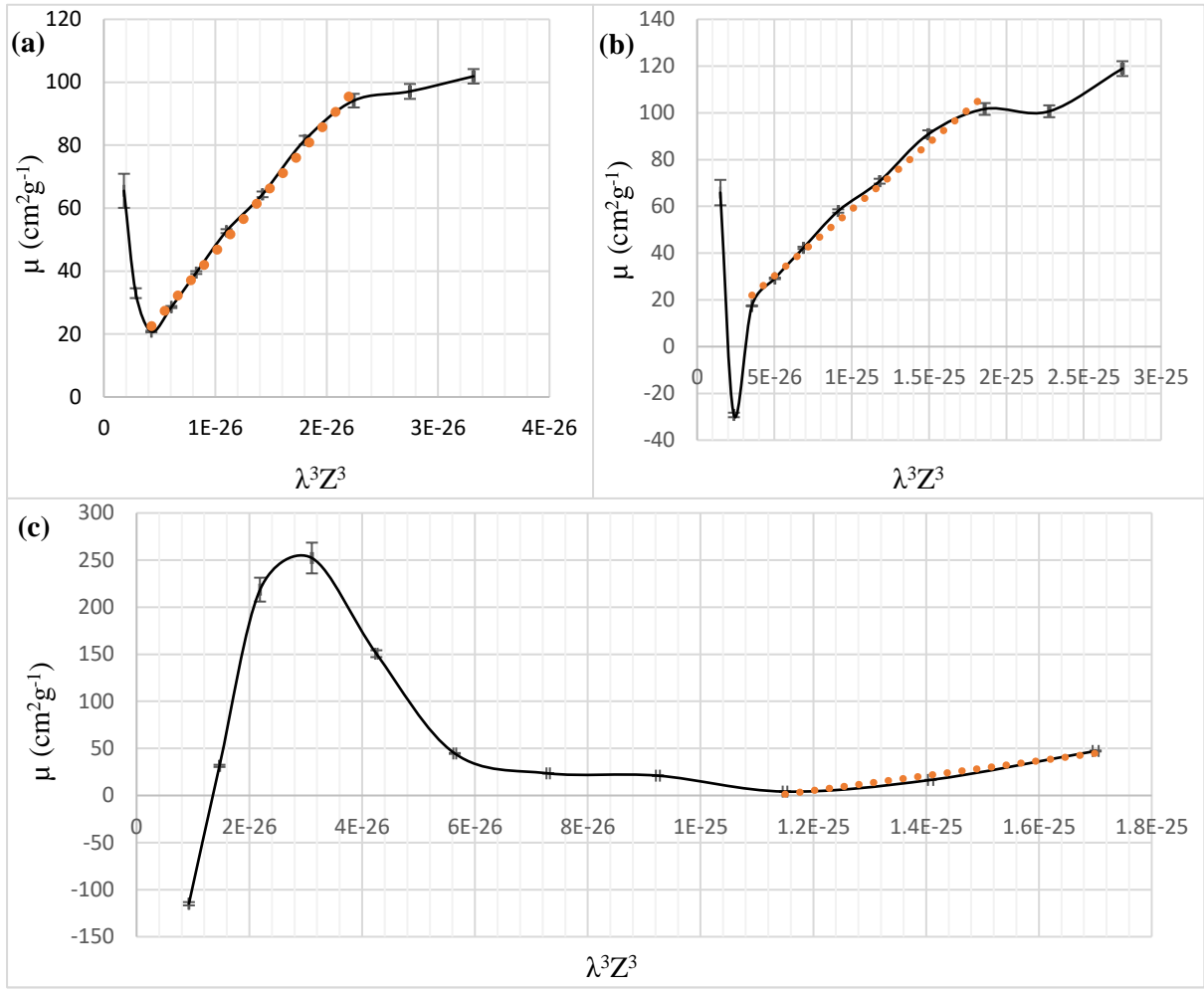
Figure 8 : Mass Absorption Coefficient μ against $\lambda^3 Z^3$ for (a) Cu (b) Ni and (c) Sn between Bragg angles $\theta = 6°$ and $\theta = 16°$ with an orange trendline highlighting the linear region over which the gradients in table 4 are calculated

The linear regions are well pronounced for Cu and Ni and the wavelength and atomic number dependency of the mass absorption coefficients of Cu and Ni show decent agreement with literature values, despite lying outside experimental errors of the literature value. Values for Sn show poor agreement with literature with an ill-defined linear region. This can be rationalised by understanding that the mass absorption coefficient only varies linearly with $\lambda^3 Z^3$ in regions away from absorption edges. Sn has a strong K-absorption edge at 29.200 keV[5] and is found within the Bragg angles used in figure 8. This is apparent in figure 8c where the absorption peaks between $(2.18 \pm 0.01) \times 10^{-26}$ m^3 and $(3.11 \pm 0.02) \times 10^{-26}$ m^3 where an absorption edge occurs. The mass absorption coefficient peaks at an absorption edge but varies rapidly below and above the edge. The $\theta = 16°$ to $\theta = 25°$ regions are largely erratic with no discernible linear region for Cu, Ni and Sn due to this existence of absorption edges.

Samples of sheet Cu, Ni, Al and Sn and powdered W, Bi, Zn and Ag were used to calculate Rydberg's constant and verify Moseley's law for K- and L-shell absorption edges. The absorption (count rate I/ background count rate I_0) was recorded between Bragg angles of $\theta = 6°$ to $\theta = 25°$. A step time of 2s was used for the powdered samples with a 5mm collimator. The sample discs were between 0.2mm and 0.4mm thick and were fastened to the end of the collimator with nothing in the sample holder. Absorption data for Cu, Ni, Al and Sn were obtained from earlier measurements. Figure 9 shows absorption against incident wavelength energies for all samples, in regions where an absorption edge was detected. The absorption edge occurs as a sharp drop in the absorption (I/I_0) as incident energy is increased and occurs due to incident wavelength energy satisfying electronic transitions.

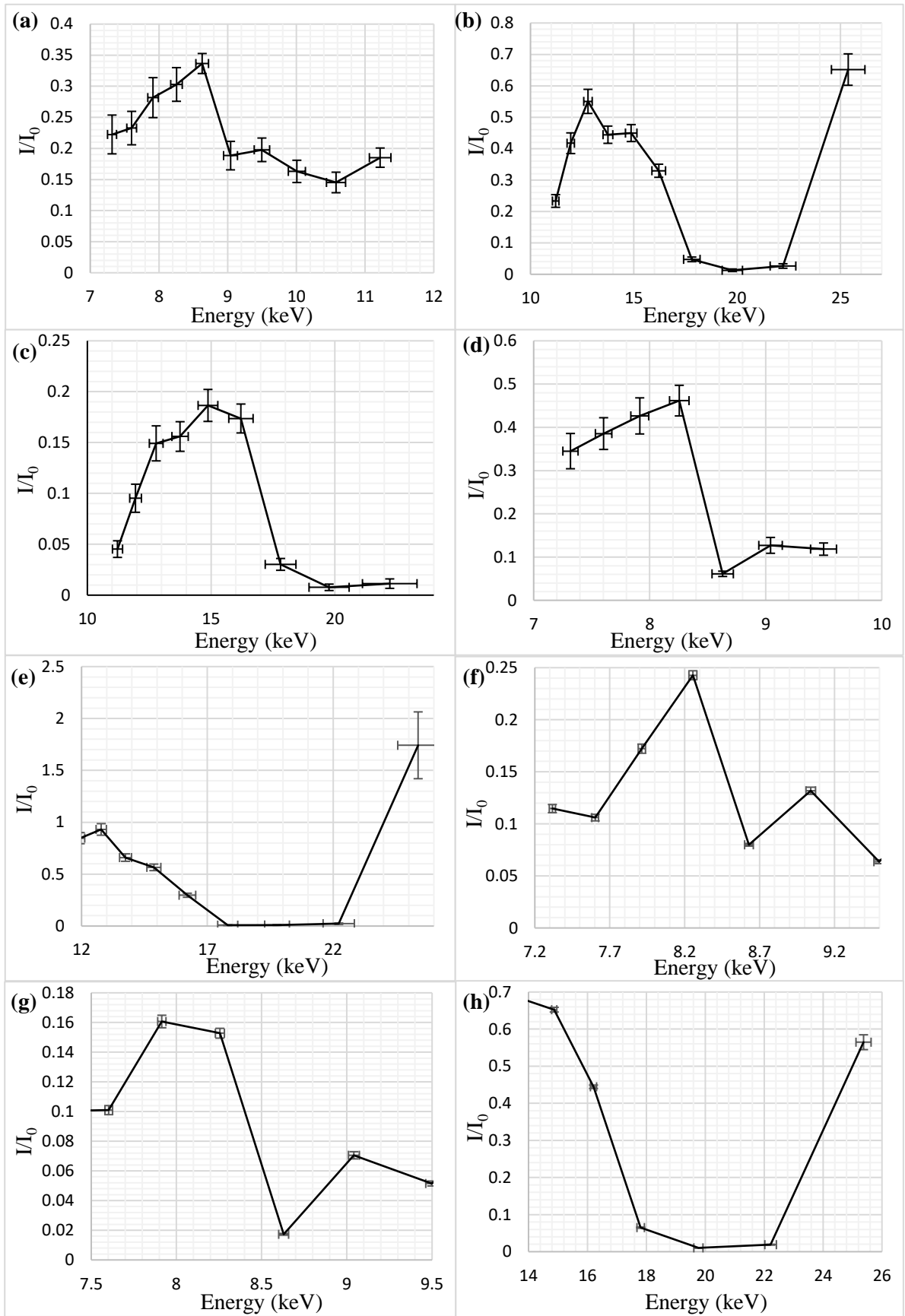Figure 9 : I/I₀ against incident energy (keV) showing absorption edges of (a)-(b) W (c) Bi (d) Zn (e) Ag (f) Cu (g) Ni and (h) Sn

The experimental absorption edges and their corresponding literature values are summarised in table 5.

Element	Experimental Value (keV)	Literature Value (keV)[9]
K-Absorption Edge		
Zn	8.6 ± 0.2	9.661
Ag	22.22 ± 0.6	25.515
Cu	8.6 ± 0.2	8.980
Ni	8.4 ± 0.1	8.331
Sn	27 ± 1	29.200
L-Absorption Edge		
W	L_1 12.0 ± 0.3	12.102
	L_3 8.8 ± 0.5	11.541
Bi	L_1 17.0 ± 0.5	16.389

Table 5 : Absorption Edge energies (keV) of K and L shell transitions compared with corresponding literature values

Decent agreement of absorption edge energies is seen with literature values. It is noted that there are three distinct edges, L_1, L_2 and L_3 in IUPAC notation, for the L-shell transitions while only one for the K-shell transition. The experimental resolution used here, however, is not high enough to accurately distinguish the three L edges.

Figure 10 shows plots of $\frac{1}{\sqrt{\lambda_E}} 10^{-4}$ against atomic number Z, where λ_E is the wavelength of the absorption edge energies outlined in table 5. Figure 10b shows a plot for the L_1 absorption edges determined in table 5.
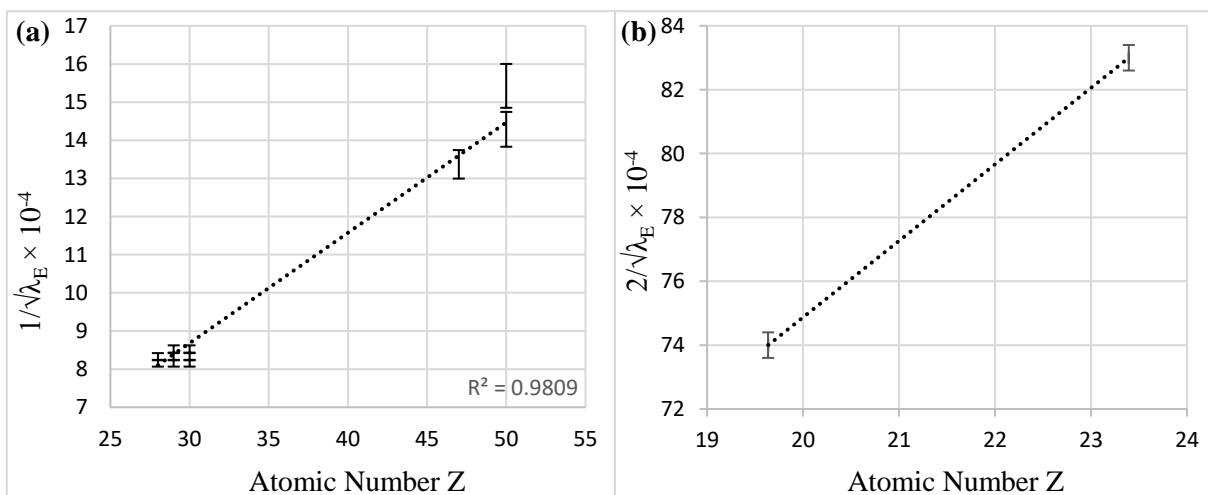

Figure 10 : (a) K and (b) L shell energies

Values for the Rydberg constant R and screening constant σ are calculated using the gradients of figures 10a and 10b with equation 7 and setting n = 1 and n = 2 for the K-shell and L-shell data respectively. Experimental Rydberg constant from K-shell calculations was determined to be $(9.3 \pm 0.4) \times 10^6$ m^{-1}

while from L-shell was determined to be $(8.7 \pm 0.3) \times 10^6$ m^{-1}. The accepted literature value is 10973731.6 m^{-1} [10]. Both values lie outside experimental errors of literature however the K-shell value is more accurate than the L-shell value.

The screening constants along with accepted literature values are outlined in table 6. Good agreement with literature is seen for the K-shell screening constant, with the value lying just within experimental error of the literature value. Very poor agreement is seen for the L-shell screening constant with accepted literature values. This can be attributed to the use of only two elements with just the L_1-edge being resolved for both.

	K-Shell σ	L-Shell σ
Experimental	1.5 ± 0.6	27 ± 5.1
Literature[11]	1	7.4

Table 6 : Screening constants σ of K-shell and L-shell compared to literature values[5]

4   Conclusions and Further Work

Herein, the mass absorption coefficients of a range of elements are calculated with decent agreement with literature values. Moseley's law is confirmed for K and $L\alpha_1$ transitions and calculations for Rydberg and screening constants are carried out. The Rydberg constant is underestimated but shows decent proximity to the literature value. Screening constant for L-shell transitions shows extremely poor agreement with literature. This is attributed to a lack of range of samples and inability to resolve the $L_{1,2,3}$ peaks. Avenues for further work include the following: measurements of the background, i.e. with nothing in the sample holder, at smaller angles ($\theta < 3°$) should return strong $K\alpha_1$ and $K\alpha_2$ peaks which can be used to obtain an effective beam width arriving at the sample. This should improve resolving power calculations. Increasing step times to obtain more precise count rate measurements should increase overall precision of results, particularly for the $L\alpha_{1,2}$ peaks of the W spectrum which could not be resolved and $L_{1,2,3}$ absorption edges of W and Bi which could also not be resolved. A greater number of elements for calculation should also return better results for the Rydberg constant and particularly the screening constant for L-shell. Additionally, the pre-prepared powder samples had air bubbles trapped within the tape, this has potentially resulted in large amounts of erroneous data.

5   References

[1]   T. Sochi, "High Throughput Software for Powder Diffraction and its Application to Heterogeneous Catalysis," Dec. 2010.

[2]   S. H. Liebson, "The discharge mechanism of self-quenching Geiger-Mueller counters," *Physical Review*, vol. 72, no. 7, pp. 602–608, 1947, doi: 10.1103/PhysRev.72.602.

[3]   K. Fukumura and S. Tsuruta, "Iron Kα Fluorescent Line Profiles from Spiral Accretion Flows in Active Galactic Nuclei," *The Astrophysical Journal*, vol. 613, no. 2, pp. 700–709, Oct. 2004, doi: 10.1086/423312.

[4]   "The London, Edinburgh and Dublin philosophical magazine and journal of science : Free Download, Borrow, and Streaming : Internet Archive." [Online]. Available: https://archive.org/details/londonedinburg6271914lond/page/n11/mode/2up. [Accessed: 20-Apr-2020].

[5]   "X-Ray Data Booklet Table 1-2. Photon energies, in electron volts, of principal K-, L-, and M-shell emission lines."

[6]   "X-ray wavelengths and x-ray atomic energy levels." [Online]. Available: https://www.mendeley.com/viewer/?fileId=24e3ce08-cdf9-792d-0217-0a02d0072e47&documentId=343b05c8-244a-3e04-9bdd-bbbfffa20196. [Accessed: 20-Apr-2020].

[7]   "Zinc - Element information, properties and uses | Periodic Table." [Online]. Available: https://www.rsc.org/periodic-table/element/30/zinc. [Accessed: 20-Apr-2020].

[8]   J. F. Cochran and D. E. Mapother, "Superconducting Transition in Aluminum," *Physical Review*, vol. 111, no. 1, pp. 132–142, Jul. 1958, doi: 10.1103/PhysRev.111.132.

[9]   "NIST: X-Ray Mass Attenuation Coefficients - Table 3." [Online]. Available: https://physics.nist.gov/PhysRefData/XrayMassCoef/tab3.html. [Accessed: 20-Apr-2020].

[10]   "CODATA Value: Rydberg constant[†]." [Online]. Available: https://physics.nist.gov/cgi-bin/cuu/Value?ryd. [Accessed: 20-Apr-2020].

[11]   C. Hohenemser and I. M. Asher, "A Simple Apparatus for Moseley's Law," *American Journal of Physics*, vol. 36, no. 10, pp. 882–885, Oct. 1968, doi: 10.1119/1.1974301.

[12]   E. L. Thomas, J. N. Millican, E. K. Okudzeto, and J. Y. Chan, "CRYSTAL GROWTH AND THE SEARCH FOR HIGHLY CORRELATED INTERMETALLICS," *Comments on Inorganic Chemistry*, vol. 27, no. 1–2, pp. 1–39, Aug. 2006, doi: 10.1080/02603590600666215.

[13]   "X Rays: Atomic Origins and Applications | Physics." [Online]. Available: https://courses.lumenlearning.com/physics/chapter/30-4-x-rays-atomic-origins-and-applications/. [Accessed: 10-Apr-2020].

[14]   "XR 4.0 expert unit Made for better education."

[15]   "NIST: X-Ray Mass Attenuation Coefficients - Aluminum." [Online]. Available: https://physics.nist.gov/PhysRefData/XrayMassCoef/ElemTab/z13.html. [Accessed: 14-Apr-2020].

[16]   "NIST: X-Ray Mass Attenuation Coefficients - Zinc." [Online]. Available: https://physics.nist.gov/PhysRefData/XrayMassCoef/ElemTab/z30.html. [Accessed: 20-Apr-2020].